Rapid determination of particle velocity from space-time images using the Radon transform

**Patrick J. Drew · Pablo Blinder · Gert Cauwenberghs ·
Andy Y. Shih · David Kleinfeld**

Abstract Laser-scanning methods are a means to observe streaming particles, such as the flow of red blood cells in a blood vessel. Typically, particle velocity is extracted from images formed from cyclically repeated line-scan data that is obtained along the center-line of the vessel; motion leads to streaks whose angle is a function of the velocity. Past methods made use of shearing or rotation of the images and a Singular Value Decomposition (SVD) to automatically estimate the average velocity in a temporal window of data. Here we present an alternative method that makes use of the Radon transform to calculate the velocity of streaming particles. We show that this method is over an order of magnitude faster than the SVD-based algorithm and is more robust to noise.

Keywords Automation · Blood flow · Brain · Kidney · Laser-scanning microscopy · Line-scan · tumor

P. J. Drew · P. Blinder · A. Y. Shih · D. Kleinfeld (✉)
Department of Physics, University of California at San Diego,
9500 Gilman Drive,
La Jolla, CA 92093, USA
e-mail: dk@physics.ucsd.edu

G. Cauwenberghs
Section on Neurobiology, University of California at San Diego,
9500 Gilman Drive,
La Jolla, CA 92093, USA

G. Cauwenberghs · D. Kleinfeld
Graduate Program in Neurosciences,
University of California at San Diego,
9500 Gilman Drive,
La Jolla, CA 92093, USA

1 Introduction

The quantification of flux of blood cells is an essential aspect of studies on neurovascular coupling under normal and pathological conditions, such as stroke and neurodegeneration (Iadecola 2004). The flux depends on both red blood cell (RBCs) velocity and the vascular diameter. Velocity is typically measured from successive line-scans using confocal or two-photon microscopy through the central axis of blood vessels after staining of the blood plasma with a fluorescent dye, while diameter is measured from by scanning perpendicular to the axis (Kleinfeld and Denk 2005; Schaffer et al. 2006; Shih et al. 2009). This results in images of time, on the ordinate, versus space on the abscissa, with bright and dark streaks that correspond to fluorescently labeled plasma and non-fluorescent RBCs, respectively (Villringer et al. 1989; Kleinfeld et al. 1998) (Fig. 1). The tangent of the angle of these streaks is inversely proportional to the velocity of RBCs in that vessel.

Past work considered a manual procedure for the determination of velocity (Zhang et al. 2005) as well as an automated procedure that made heavy use of the singular valued decomposition (SVD) (Kleinfeld et al. 1998). In the latter method, the temporal scale, t, is rescaled as $t \leftarrow t + x/c$ where x is the spatial scale. The value and sign of the speed, c, that produces horizontal rather than angled streaks will correspond to the best estimate of the velocity. The optimum estimate corresponds to a singular space-time data matrix, or a maximally singular matrix in the presence of noise and fluctuations in flow. While this method enjoys use to quantify blood cell velocity in brain (Kleinfeld et al. 1998; Chaigneau et al. 2003; Hutchinson et al. 2006; Schaffer et al. 2006; Nishimura et al. 2007; Stefanovic et al. 2007; Petzold et al. 2008; Shih et al. 2009), kidney (Kang et al. 2006), and tumors (Fukumura and Jain 2008),
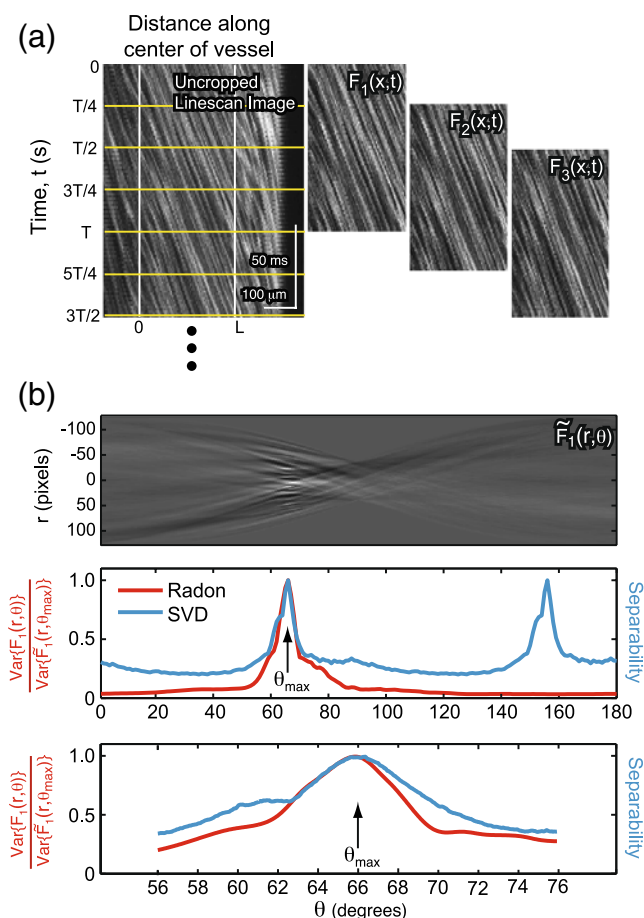
Fig. 1 Illustration of Radon method to determine RBC velocity. (**a**) Raw line-scan image data. *White, vertical lines* show the spatial range selected for analysis. The *yellow lines* show the temporal windowing. The data blocks to the right are overlapping windows of data that are ready for processing, denoted F_i (x, t) where i is an index in units of T/4, where T is the duration of the data block and L is the length of the useable line-scan (Eq. (1)). (**b**) The *top* image shows the Radon transform of first data block (Eq. (2)). The plot below shows the normalized variance (Eq. (3)) of the Radon transform in *red*. The *blue trace* is the normalized separability index obtained using the SVD method as a function of rotation angle using the same window of data. Though both methods show a peak at 65º, the SVD separability index has a second peak at 155º. Insert shows an enlargement of the peaks at 65º

estimation of singular values is time consuming and velocity cannot be estimated in real-time with current computer speeds. Further, the SVD-based method is prone to failure under stalls in flow.

Here, we describe an alternative means to find the velocity that makes use of the Radon transform (Deans 1983; Averbuch et al. 2001), which takes a set of line integrals along the image at different tangents. The Radon transform is a variant of the generalized Hough transform (Gotze and Druckmuller 1996; O'Brien et al. 2003) that is commonly used in computer vision applications. By finding the angle with maximal variance in the Radon transform, we can estimate the velocity of the particle. We expect that

it may be computationally superior to the past, SVD-based method. The time to complete a Radon transform of a data set asymptotically varies as the number of pixels (Ballard 1981), while the past method requires repeated rescaling of a data matrix, followed by calculation of the SVD of the rescaled matrix; the latter step varies as the number of pixels *times* the smallest dimension or rank of the data set (Golub and Kahan 1965).

2 Methods

2.1 Experimental methods

Male Sprague-Dawley rats, 270 to 310 g in mass, were used in accordance with both the local IACUC and NIH regulations. Detailed surgical procedures are described elsewhere (Helmchen and Kleinfeld 2008; Shih et al. 2009). In brief, anesthesia was maintained with 1 to 2 % (*v/v*) isoflurane in 30% (*v/v*) oxygen and 70% (*v/v*) nitrous oxide. Cranial windows, 4×4 mm in size and centered at 4.5 mm lateral and −3.0 mm caudal, were constructed as described previously (Kleinfeld et al. 2008). Images were collected using a two-photon laser scanning microscope of local design (Tsai et al. 2002, 2003; Tsai and Kleinfeld 2009) that was controlled by MPScope software (Nguyen et al. 2006, 2009). The vasculature was visualized by circulating 2MDa fluorescein-dextran (FD2000S, Sigma), as described previously (Schaffer et al. 2006). The flow of RBCs is visualized as dark objects against the fluorescent plasma background. A 40x magnification water-dipping objective (Olympus America, Center Valley, PA) was used to obtain the line-scan data. Scans were collected along the centerline of each vessel over a length of 70 to 250 pixels, which spanned 7 to 76 µm, at a scan rate of 1.6 kHz per line.

2.2 Windowing and normalization of line-scan data

The raw data consists of successive line-scans along the central axis of an arteriole lumen (Fig. 1(a)). The spatial dimension, x, corresponds to the linear motion of the focal volume along the blood vessel. The required resolution along x is set by the diffraction limit. For a 40-X water-dipping lens, the lateral resolution is about 0.7 µm, yielding a sampling of $\Delta x \approx 0.3$ µm per pixel. For a typical 150 µm field, this requires ~ 500 samples per line. At the ~ 500 µs per line scan rate of high-speed gravimeter mirror scanners (model 6110, Cambridge Technology, Lexington, MA), the sampling time is thus $\Delta t \approx 1$ µs per pixel. An upper limit to the maximum velocity that can be determined with scanning measurements is set by $(\frac{1}{2})\Delta x/\Delta t \approx 150$ mm/s; the factor of ½

results from the use bidirectional scanning to correct for the speed of the scan mirrors. Signal-to-noise constraints may necessitate the use of slower scan rates, as discussed (Tsai and Kleinfeld 2009).

From the continuous data set of Fig. 1(a), we select a strip along x that contains a straight, planar section of the vessel. We define this width as $L \equiv N_x \Delta x$, where N_x is the number of spatial samples; typically, $L \sim 40$ μm. We window the data in time intervals of $T = N_t \Delta t$ separate windows, where N_t is the number of lines in the sample. We calculate the velocity for successive blocks of the windowed line-scan data, with an overlap of T/4 between blocks. Each block is denoted $F_i(x, t)$ where i is an index that corresponds to time in units of T/4. The Nyquist frequency is $(2T)^{-1}$, or 10 Hz for the typical choice of T= 50 ms; this is sufficient to capture the heart-rate of the rat without aliasing.

Each windowed data block is first normalized to remove inhomogeneities in illumination in space and to remove the baseline intensity, usually using the first second, 20T of data, so that the data block has a mean value of zero, i.e.,

$$F_i(x, t) \leftarrow F_i(x, t) - \frac{1}{20T}$$
$$\times \sum_{j=1}^{20} \int_0^T dt\, F_j(x,t) - \frac{1}{LT} \int_0^L dx \int_0^T dt\, F_i(x,t). \tag{1}$$

The Radon transform maps each windowed data block F_i (x, t) from space-time coordinates to space-velocity coordinates, $\widetilde{F}_i(r, \theta)$, by

$$\widetilde{F}_i(r, \theta) = \frac{1}{LT} \int_0^L dx \int_0^T dt\, F_i(x, t)\delta\left(r - \frac{x}{\Delta x}\cos\theta - \frac{t}{\Delta t}\sin\theta\right). \tag{2}$$

Bright points in the transformed data correspond to lines at particular angles and radii (Fig. 1(b)). If the original image block $F_i(x, t)$ contains many streaks with a similar orientation, as produced by a line-scan along a blood vessel, the variance of $\widetilde{F}_i(r, \theta)$ along r is maximal along the orientation of the streaks.

2.3 Radon-based algorithm

All analyses were executed in 32-bit MatLab™ (Version 7.5.0 R2007b, Mathworks, Natick, MA); the Radon function is present in the Image Processing Toolbox. The velocity corresponds to the angle, θ_{max}, for which the

variance of $\widetilde{F}_i(r, \theta)$ along the radius, r, for a given transform angle, θ, is a maximum, where

$$\mathrm{Var}\left\{\widetilde{F}_i(r,\ \theta)\right\}_r \equiv \frac{1}{\sqrt{N_x^2 + N_t^2}} \sum_{r=1}^{\sqrt{N_x^2+N_t^2}} \widetilde{F}_i^2(r, \theta). \tag{3}$$

The limits N_x and N_t are distances, in pixels, in the space and time dimensions, respectively, for the angle θ. Once the angle with maximal variance, θ_{max}, is determined for each block (Eq. (3)), the velocity V_i for the data block i (Fig. 2, middle trace) is given by

$$V_i(\theta_{max}) = \frac{\Delta x}{\Delta t} \cot(\theta_{max}). \tag{4}$$

The domain of θ_{max} is (−90°, 90°) for the velocity range (−∞, +∞), so that each velocity gives rise to a unique peak in θ.

We boot-strapped the data to obtain an estimate of the signal-to-noise ratio (S/N) for velocity at for each block. If the angle of maximal variance is θ_{max}, then the S/N for the best estimate of the velocity, denoted $S_i(\theta_{max})$, is itself estimated by

$$S_i(\theta_{max}) = \frac{\mathrm{Var}\left\{\widetilde{F}_i(r, \theta_{max})\right\}_r}{\frac{1}{N}\sum_{k=1}^{N}\mathrm{Var}\left\{\widetilde{F}_i(r, \theta_{k*180/N})\right\}_r}. \tag{5}$$

For the choice N=12, we find empirically that a $S_i(\theta_{max}) \geq$ 3 is necessary for accurate detection. Good line-scan data can
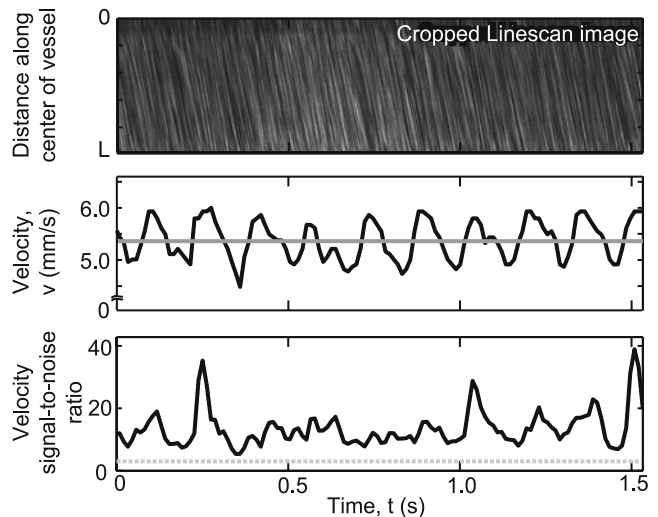
Fig. 2 Radon-based analysis of spatially windowed line-scan data. *Top*, spatially windowed raw line-scan data. Center, plot of the velocity versus time (*black*) (Eq. (4)), *grey line* shows the mean velocity. The variation of the velocity occurs at the heart-rate. *Bottom*, plot of the signal-to-noise for the radon-based estimate of velocity (Eq. (5)). *Dotted gray line* shows empirical threshold for acceptable data

have average $S_i(\theta_{max})$ in the range of 10 to 20 and with a clearly visible heartbeat both in the power spectrum and the velocity trace. Time points with $S_i(\theta_{max}) < 3$ were flagged and velocity values interpolated between the last and next points with signal-to-noise greater than 3.

2.4 SVD-based algorithm

We used a rotation variant of the implementation of the SVD-based algorithm (Schaffer et al. 2006), with nearest-neighbor interpolation, to compare the Radon-based against the SVD-based algorithm. Cropped data windows (Fig. 1(a)) were already square, i.e., the number of points in the time axis is the same as in the space axis, and thus did not require rescaling, and windows were rotated at various angles in a preset range between 0° and 90°. The separability index is given by the ratio of the magnitude of the power for the mode with the largest singular value, denoted λ_o, to the sum of the magnitudes of the power in all modes (Kleinfeld et al. 1998; Schaffer et al. 2006), i.e., index $= \sum_n^{\text{all modes}} \lambda_o^2/\lambda_n^2$.

2.5 Quantification of error in the presence of noise

To quantify the effects of noise on the angle estimate, we used the equation

$$E_j = \sqrt{\sum_{t=0}^{T} \left(\theta_0(t) - \theta_j(t)\right)^2} \qquad (6)$$

where E_j is the error for noise level j, $\theta_0(t)$ is the estimate of the angle in the noiseless case, $\theta_j(t)$ is the estimate of the angle for the noise level j, and t is the time step.

The equations for the artificial line-scan data, i.e., $F(x, t)$ generated in Fig. 3, are given by

$$\phi(x) = 2\pi \tfrac{1}{50} x$$
$$\omega(t) = 30 + \sin(0.0132\, t) \qquad (7)$$
$$F(x, t) = \tfrac{1}{2}\left\{1 + \sin\left[\tfrac{2\pi}{1000}\omega(t) + \phi(x)\right]\right\}$$

with the arbitrary units (AUs) of x running from 1 to 96 and those of t from1 to 1536. Note that parameters for the above equations were empirically chosen to generate a range of angles for demonstration purposes.

3 Results

3.1 Extraction of velocity from line-scan data

We consider windowed line-scan data from an arteriole (Fig. 1(a)). Streaks, caused by RBCs moving in the fluorescein labeled plasma, are clearly visible. The

relevant spatial limits of the line-scan are selected by hand. The transform of the data into Radon space $\tilde{F}_i(r, \theta)$, is shown in the top panel of Fig. 1(b). There are more extremes of light and dark, and thus higher variance, along the angle corresponding to ~65°. The variance in space for each angle, normalized to the maximal variance, is shown in the middle trace of Fig. 1(b) in red. We observe a single, well defined maximum.

For comparison between the Radon-based and SVD-based methods, the normalized separability index for the SVD-based analysis of the same window of data is shown in blue (Fig. 1(b)). Both measures show peaks at ~ 65°, so that their best estimate of the velocity are in agreement. The peak is sharper for the Radon method; middle trace of Fig. 1(b). Note, however, that the SVD separability index shows a second, spurious peak shifted by 90°; this corresponds to vertical as well as horizontal stripes.

We now return to the full data set and consider the progression of velocity across overlapping windows (Fig. 2) using the Radon-method. The velocity estimate along several seconds of line scan data clearly shows the ~6 Hz heartbeat oscillation (Fig. 2, middle trace). An instantaneous estimate of the signal-to-noise ratio for the velocity (Eq. (5)) over the same time period shows a variable but high ratio (Fig. 2, bottom trace). In practice, we set a velocity S/N of 3 as being the lower cutoff (Fig. 2, dotted line in bottom trace). In this form of data, high quality records will have a velocity S/N over 10, with oscillations in the velocity at the heart rate clearly visible.

3.2 Robustness to noise

We quantified the accuracy of the Radon- and SVD-based methods under different signal-to-noise regimes for simulated raw data. For this purpose, we generated simulated data and degraded it with additive exponential noise to reproduce the noise characteristically observed in our two photon imaging system (Tsai et al. 2002). The low noise case (Fig. 3(a) top) is comparable to typical best data, the high noise (Fig. 3(a), bottom) comparable to that obtained imaging several hundred microns below the cortical surface. The SVD-based method was restricted to a range of angles between 0° and 90°. To quantify the error, we looked at the standard deviation in the angle estimate as the noise increased (Eq. (6)). The estimates of angle for the same simulated data using the Radon- and SVD-based methods are shown in Fig. 3(b). As the noise increases, both methods lose accuracy. At all levels of noise, the standard deviation in the SVD-based estimate were higher than the Radon estimates, sometimes by as much as an order of magnitude (Fig. 3(c)). Thus the Radon transform is more robust to noise than singular value decomposition. Note that the plot shows angle, not velocity. For angles near
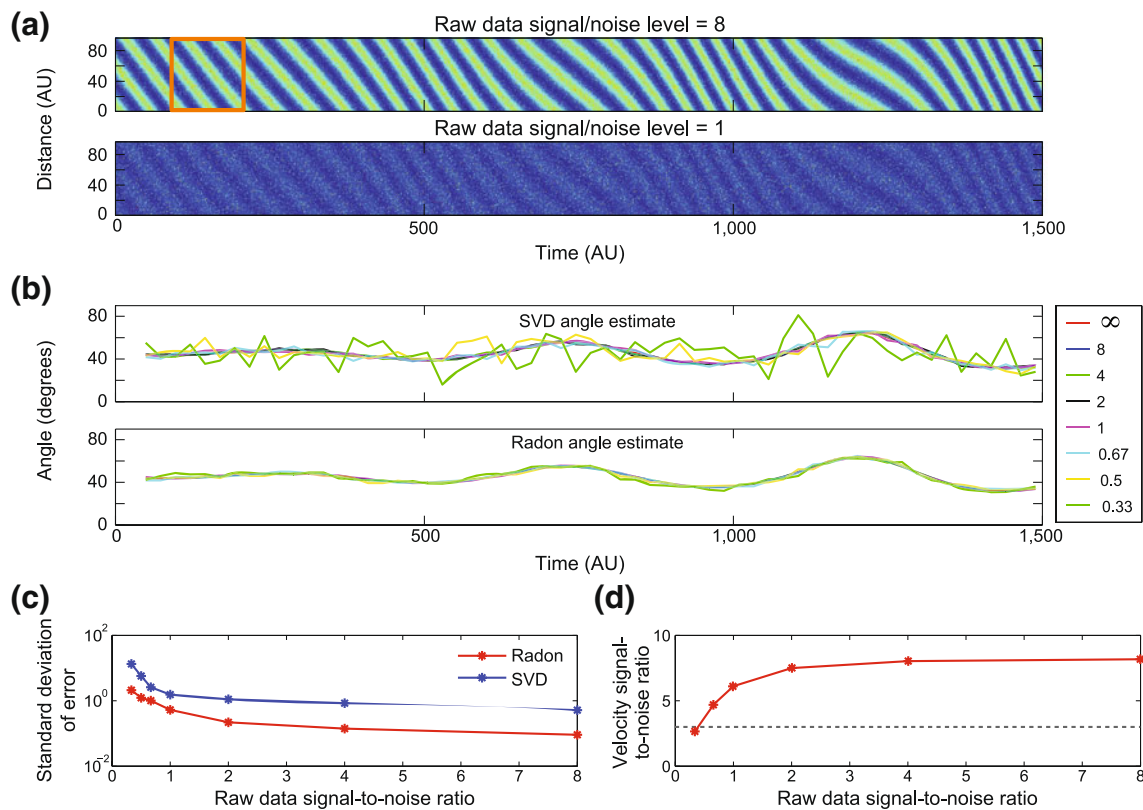
Fig. 3 Effects of noise on Radon- and SVD-based determinations of angle. (**a**) *Top*, simulated data with a low level of exponential additive noise, with mean 0.125 of signal amplitude. *Bottom*, simulated data with a high level of exponential additive noise, with mean equal to signal amplitude. Color maps have been scaled to match the range of the data. *Orange square* shows the extent of size of a window of data. (**b**) Estimates of angle of data versus time using SVD-based method (*top*) and Radon-based (*bottom*) for varying levels of noise. Estimates were done over 96×96 pixel windows with a 24 line overlap. Calculations were nonadaptive, *i.e.*, angle from previous window was not used as a seed). (**c**) Standard deviation in the angle estimate introduced by noise (Eq. (6)) for Radon (*red*) and SVD-based (*blue*) methods. Standard deviation in the angle estimate at each noise level is calculated by taking the square root sum of squared difference between angles in the zero-noise simulated data and the data with additive exponential noise. (**d**) Signal-to-noise ratio of the Radon-based estimate for the velocity (Eq. (5)) versus signal-to-noise ratio for simulated data. *Red dotted line* shows a velocity S/N of 3, the empirical determined cutoff we use for experimental data. The velocity S/N drops sharply when the raw data S/N of 1 falls below 1

zero, such as those obtained from scanning fast flow in an artery, small changes in angle translate to large changes in velocity, magnifying the error.

Qualitatively, the Radon method only fails when the lines in the image are no longer visible to the naked eye. Other forms of noise, *i.e.*, Gaussian additive and multiplicative, were observed to have similar effects (not shown). The signal-to-noise ratio for the velocity estimate (Eq. (5)) is seen to increase as a function of the S/N of the simulated data (Fig. 3(d)). The score plateaus as the lines in the simulated data have nonzero thickness similar to that caused by the occlusion of dye by blood cells; thinner lines result in a higher plateau (not shown). Lastly, use of the Radon transform also allows accurate estimates of velocity with temporally decimated data. Accurate estimates of speeds can be made so long as the angles of the streaks remains relatively separated from the horizontal, *i.e.*, ~ 10° (data not shown).

For a pure, noiseless signal, i.e. a purely spatially or purely temporally modulated grating, the first mode will

contain the entirety of the signal. However, in practice, the angle of streaks within a window of data, either real and simulated, is constantly changing due to tumbling of RBCs or slight changes in velocity (Figs. 2 and 3); thus there will be multiple non-zero modes even in a 'noiseless' image, decreasing the separability. The addition of noise only increases the power in these modes.

3.3 Execution speed

As a means to increase the execution speed of the algorithm, we exploit the observation that the angle of the streaks in arteriole data do not change very rapidly. This allows use of an adaptive algorithm that searches in a subset of angles using the previous angle as a starting point. For the first window of data, the Radon transform is performed for θ varying from 1° to 180°. We calculate the variance of $\tilde{F}_i(r, \theta)$ along r for each value of θ. We recalculate the Radon transform for a smaller range of angles, usually ± 3° with a 0.25° increment, around

the angle with maximal variance to get a stringent estimate of the true velocity. Once this is completed for the first window, it can be performed adaptively by only searching ± 10° around the last angle before repeating the finer grained search. If the angle estimate is greater than 8° away from the estimate of the previous time point, the adaptive algorithm iteratively searches for the peak to avoid local minima.

With the above adaptive algorithm, with data block sizes appropriate for real data, i.e., approximately 100 by 100 pixels, we found the Radon method was ~25 times faster than the SVD-based method. The Radon method allowed us to complete an analysis in a time similar to the acquisition time, *i.e.*, adaptive analysis of a 100 point in space by 30,000 point in time data-set, about a 12 s interval, is complete in 16 s on a 2.3 GHz processor. The relative improvement of the Radon method over the SVD-based method is expected to increase for larger data sets. With matrices whose sizes were appropriate for real data, approximately 2/3 of the computational time was spent performing the rotation while the remaining 1/3 of the time was spent calculating the SVD per se (not shown). The time for the rotation as well as the Radon transform of a N x N matrix both scale as N^2, while the time for a SVD scales as N^3 (Golub and Kahan 1965).

4 Conclusion

We present an improved method for determination of particle velocity from space-time plots using the Radon transform. It is more than an order of magnitude faster than the previous standard method. It is also more resistant to noise as it makes use of the spatial order of the line-scan data. This allows accurate velocity measurement under conditions with low signal-to-noise ratios, such as when imaging deep into tissue. Use of the Radon method should also enable the use of complicated line-scan trajectories (Göbel et al. 2007), allowing velocity measurements from multiple vessels, albeit at a lower temporal resolution. Unlike other particle-velocity estimation methods using spatiotemporal autocorrelations (Sourice and Plantier 2005), the Radon-based method requires no fitting of arbitrary functions. Though we focus on data obtained from vessels in the brain using two-photon microscopy, the method presented here should be broadly applicable to all types of line-scan data, including that obtained from microfluidic channels (Chao et al. 2005).

References

Averbuch, A., Coifman, R. R., Donoho, D. L., Israeli, M., & Walden, J. (2001). Fast slant stack: A notion of radon transform for data on a cartesian grid which is rapidly computable, algebraically exact, geometrically faithful, and invertible. In: Technical Report (University S, ed).

Ballard, D. H. (1981). Generalizing the Hough transform to detect arbitrary shapes. *Pattern Recognition, 13*, 111–122. doi:10.1016/0031-3203(81)90009-1.

Chaigneau, E., Oheim, M., Audinat, E., & Charpak, S. (2003). Two-photon imaging of capillary blood flow in olfactory bulb glomeruli. *Proceedings of the National Academy of Sciences of the United States of America, 100*, 13081–13086. doi:10.1073/pnas.2133652100.

Chao, S. H., Holl, M. R., Koschwanez, J. H., Carlson, R. H., Jang, L. S., & Meldrum, D. R. (2005). Velocity measurement in micro-channels with a laser confocal microscope and particle linear image velocimetry. *Microfluidics and Nanofluidics, 1*, 155–160. doi:10.1007/s10404-004-0023-6.

Deans, S. R. (1983). *The Radon transform and some of its applications*. New York: Wiley and Sons.

Fukumura, D., & Jain, R. K. (2008). Imaging angiogenesis and the microenvironment. *Acta Pathologica, Microbiologica et Immunologica Scandinavica, 116*, 695–715.

Göbel, W., Kampa, B. M., & Helmchen, F. (2007). Imaging cellular network dynamics in three dimensions using fast 3D laser scanning. *Nature Methods, 4*, 73–79. doi:10.1038/nmeth989.

Golub, G. H., & Kahan, W. (1965). *Calculating singular values and pseudo-inverse of a matrix*. Philadelphia: Society for Industrial and Applied Mathematics.

Gotze, W. A., & Druckmuller, H. J. (1996). A fast digital Radon transform–an efficient means for evaluating the Hough transform. *Pattern Recognition, 28*, 1985–2992.

Helmchen, F., & Kleinfeld, D. (2008). *In vivo* measurements of blood flow and glial cell function with two-photon laser scanning microscopy. *Methods in Enzymology, 444*, 231–254. doi:10.1016/S0076-6879(08)02810-3.

Hutchinson, E. B., Stefanovic, B., Koretsky, A. P., & Silva, A. C. (2006). Spatial flow-volume dissociation of the cerebral microcirculatory response to mild hypercapnia. *NeuroImage, 32*, 520–530. doi:10.1016/j.neuroimage.2006.03.033.

Iadecola, C. (2004). Neurovascular regulation in the normal brain and in Alzheimer's disease. *Nature Reviews. Neuroscience, 5*, 347–360. doi:10.1038/nrn1387.

Kang, J. J., Toma, I., Sipos, A., McCulloch, F., & Peti-Peterd, J. (2006). Quantitative imaging of basic functions in renal (patho) physiology. *American Journal of Physiology. Renal Physiology, 291*, F495–F502. doi:10.1152/ajprenal.00521.2005.

Kleinfeld, D., & Denk, W. (2005). Imaging in neuroscience and development. In R. Yuste & A. Konnerth (Eds.), *Two-photon imaging of cortical microcirculation* (pp. 701–705). Cold Spring Harbor: Cold Spring Harbor Laboratory Press.

Kleinfeld, D., Mitra, P. P., Helmchen, F., & Denk, W. (1998). Fluctuations and stimulus-induced changes in blood flow observed in individual capillaries in layers 2 through 4 of rat neocortex. *Proceedings of the National Academy of Sciences of the United States of America, 95*, 15741–15746. doi:10.1073/pnas.95.26.15741.

Kleinfeld, D., Friedman, B., Lyden, P. D., & Shih, A. Y. (2008). Animal models of acute neurological injuries. In J. Chen, Z. Xu, X.-M. Xu & J. Zhang (Eds.), *Targeted occlusion to surface and deep vessels in neocortex via linear and nonlinear optical absorption*. Totowa: Humana.

Nguyen, Q.-T., Tsai, P. S., & Kleinfeld, D. (2006). MPScope: a versatile software suite for multiphoton microscopy. *Journal of*

Neuroscience Methods, 156, 351–359. doi:10.1016/j.jneumeth.2006.03.001.

Nguyen, Q.-T., Dolnick, E. M., Driscoll, J., & Kleinfeld, D. (2009). Methods for *in vivo* optical imaging. In R. D. Frostig (Ed.), *MPScope 2.0: A computer system for two-photon laser scanning microscopy with concurrent plasma-mediated ablation and electrophysiology* (2nd ed., pp. 117–142). Boca Raton: CRC.

Nishimura, B., Schaffer, C. B., Friedman, B., Lyden, P. D., & Kleinfeld, D. (2007). Penetrating arterioles are a bottleneck in the perfusion of neocortex. *Proceedings of the National Academy of Sciences of the United States of America, 104*, 365–370. doi:10.1073/pnas.0609551104.

O'Brien, J. T., Erkinjuntti, T., Reisberg, B., Roman, G., Sawada, T., Pantoni, L., et al. (2003). Vascular cognitive impairment. *The Lancet Neurology, 2*, 89–98. doi:10.1016/S1474-4422(03)00305-3.

Petzold, G. C., Albeanu, D. F., Sato, T. F., & Murthy, V. N. (2008). Coupling of neural activity to blood flow in olfactory glomeruli is mediated by astrocytic pathways. *Neuron, 58*, 879–910. doi:10.1016/j.neuron.2008.04.029.

Schaffer, C. B., Friedman, B., Nishimura, N., Schroeder, L. F., Tsai, P. S., Ebner, F. F., et al. (2006). Two-photon imaging of cortical surface microvessels reveals a robust redistribution in blood flow after vascular occlusion. *Public Library of Science Biology, 4*, 258–270.

Shih, A.Y., Friedman, B., Drew, P. J., Tsai, P. S., Lyden, P. D., & Kleinfeld, D. (2009). Active dilation of penetrating arterioles restores red blood cell flux to penumbral neocortex after focal stroke. *Journal of Cerebral Blood Flow and Metabolism, 29*, 738-751. doi:10.1038/jcbfm.2008.166.

Source, A., & Plantier, G. (2005). Red blood cell velocity estimation in microvessels using the spatiotemporal autocorrelation. *Measurement Science & Technology, 16*, 2229–2239. doi:10.1088/0957-0233/16/11/014.

Stefanovic, B., Hutchinson, E., Yakovleva, V., Schram, V., Russell, J. T., Belluscio, L., et al. (2007). Functional reactivity of cerebral capillaries. *Journal of Cerebral Blood Flow and Metabolism, 28*, 961–972. doi:10.1038/sj.jcbfm.9600590.

Tsai, P. S., & Kleinfeld, D. (2009). Methods for *in vivo* optical imaging. In R. D. Frostig (Ed.), *In vivo two-photon laser scanning microscopy with concurrent plasma-mediated ablation: Principles and hardware realization* (2nd ed., pp. 59–115). Boca Raton: CRC.

Tsai, P. S., Nishimura, N., Yoder, E. J., Dolnick, E. M., White, G. A., & Kleinfeld, D. (2002). *In vivo* optical imaging of brain function. In R. D. Frostig (Ed.), *Principles, design, and construction of a two photon laser scanning microscope for in vitro and in vivo brain imaging* (pp. 113–171). Boca Raton: CRC.

Tsai, P. S., Friedman, B., Ifarraguerri, A. I., Thompson, B. D., Lev-Ram, V., Schaffer, C. B., et al. (2003). All-optical histology using ultrashort laser pulses. *Neuron, 39*, 27–41. doi:10.1016/S0896-6273(03)00370-2.

Villringer, A., Haberl, R. L., Dirnagl, U., Anneser, F., Verst, M., & Einhaupl, K. M. (1989). Confocal laser microscopy to study microcirculation on the rat brain surface *in vivo*. *Brain Research, 504*, 159–160. doi:10.1016/0006-8993(89)91616-8.

Zhang, S., Boyd, J., Delaney, K., & Murphy, T. H. (2005). Rapid reversible changes in dendritic spine structure *in vivo* gated by the degree of ischemia. *The Journal of Neuroscience, 25*, 5333–5338. doi:10.1523/JNEUROSCI.1085-05.2005.